Black-hole kicks from numerical-relativity surrogate models

Davide Gerosa, François Hébert, and Leo C. Stein

Black-hole kicks from numerical-relativity surrogate models

Davide Gerosa,[*] François Hébert,[†] and Leo C. Stein[‡]
TAPIR 350-17, California Institute of Technology,
1200 E California Boulevard, Pasadena, CA 91125, USA

Binary black holes radiate linear momentum in gravitational waves as they merge. Recoils imparted to the black-hole remnant can reach thousands of km/s, thus ejecting black holes from their host galaxies. We exploit recent advances in gravitational waveform modeling to quickly and reliably extract recoils imparted to generic, precessing, black hole binaries. Our procedure uses a numerical-relativity surrogate model to obtain the gravitational waveform given a set of binary parameters, then from this waveform we directly integrate the gravitational-wave linear momentum flux. This entirely bypasses the need of fitting formulae which are typically used to model black-hole recoils in astrophysical contexts. We provide a thorough exploration of the black-hole kick phenomenology in the parameter space, summarizing and extending previous numerical results on the topic. Our extraction procedure is made publicly available as a module for the Python programming language named SURRKICK. Kick evaluations take ~ 0.1 s on a standard off-the-shelf machine, thus making our code ideal to be ported to large-scale astrophysical studies.

I. INTRODUCTION

Gravitational waves (GWs) carry energy, linear momentum, and angular momentum, and are therefore responsible for the final evolutionary stages of compact binary systems. As energy and angular momentum are dissipated away, the two objects inspiral and eventually merge. The GW-driven orbital decay of two neutron stars was first observed by pulsar timing, leading to a major confirmation of Einstein's theory of general relativity [1]. The first landmark detection of GWs was from a binary black hole (BH) which was brought to merger by those same GWs that ultimately reached our detectors [2].

Much like dissipation of energy and angular momentum causes the orbit of a BH binary to shrink, emission of linear momentum through GWs causes the binary's center of mass to recoil [3, 4]. The key property to generate a GW recoil (or "kick") is asymmetry. It is straightforward to show that symmetry prevents linear momentum dissipation during inspiral and merger of equal-mass, nonspinning BHs. Conversely, a generic BH binary radiates GWs anisotropically: linear momentum is preferentially emitted in some direction, and the binary consequently recoils. BH kicks were first studied using the post-Newtonian (PN) approximation (e.g. [5–7]) but their full astrophysical relevance was only realized after numerical relativity (NR) simulations of BH mergers became possible [8–10]. Most of the linear momentum is emitted during the last few orbits and merger, which corresponds to the highly dynamical, fully non-linear regime that can only be captured with NR simulations.

In particular, simulations showed that BHs formed following a merger may be imparted recoil velocities of up to 5000 km/s [11–14]. The striking astrophysical conse-

quences of these findings were quickly realized (e.g. [15–20]): BH recoils might exceed the escape speed of even the most massive galaxies in the Universe [21, 22] thus making galactic ejections a possible outcome of binary mergers [23]. Recoiling BHs might give rise to a variety of electromagnetic signatures [24] —notably a kinematical offset of a set of broad emission lines— which led to the identifications of a few observational candidates [25–31] (see also [32–34] for detection strategies). As the system recoils, a Doppler shift of the emitted GWs can provide a possible direct observational signature of BH kicks within the reach of future space- and ground-based GW observatories [35].

Since NR simulations are far too expensive to be performed in astrophysical population studies, BH kicks have mostly been modeled using fitting formulae based on PN theory and calibrated to NR simulations (e.g. [36–40]). These "black box" expressions return the final kick of the BH remnant given the intrinsic parameters (mass ratio and spins) of the merging binary at some initial separation. Another, so far unexplored, possibility to model BH kicks is to compute the flux of linear momentum in GWs using a waveform approximant that can be quickly evaluated in parameter space. Linear momentum dissipation, however, is encoded in both differences between the dominant $l = 2, m = \pm 2$ modes and higher harmonics ($l > 2$) [41]. This approach, therefore, requires an inspiral-merger-ringdown approximant able to model both higher harmonics (crucial to linear momentum flux) and misaligned spins (which are known to generate the largest kicks).

In this paper we present the first attempt in this direction using the recent NR surrogate model by Blackman *et al.* [42] — the first waveform approximant able to model generic precessing systems with higher harmonics. In contrast with the available fitting formulae, our procedure provides not only the final kick speed v_k, but also the entire velocity accumulation profile $\mathbf{v}(t)$. We present a thorough exploration of BH recoils for generic systems, which summarizes and extends various previous findings

—————
[*] Einstein Fellow; dgerosa@caltech.edu
[†] fhebert@caltech.edu
[‡] leostein@tapir.caltech.edu

in a coherent fashion. Our numerical code, SURRKICK, is publicly available and allows for reliable computation of the radiated quantities (energy, linear momentum, and angular momentum) at a moderate computational cost. Our implementation is therefore ideal to be ported to larger-scale astrophysical codes which require fast estimates of BH kicks, such as galaxy merger-tree simulations, populations synthesis studies, and GW event rates predictions.

This paper is organized as follows. Sec. II introduces the main tools of our analysis; Sec. III presents results and comparisons with other methods; Sec. IV explores the numerical accuracy of our procedure; Sec. V briefly describes implementation and usage of our public code; Sec. VI draws conclusions and future prospects. Unless otherwise stated, we use relativists' units $c = G = 1$.

II. METHODS

A. Numerical-relativity surrogate models

Surrogate models interpolate a set of precomputed GW signals and make use of advanced decomposition and interpolation schemes to quickly produce waveforms for any desired point in parameter space. Surrogate models are typically optimized to accurately reproduce the complex gravitational-wave strain, here expanded in terms of spin-weighted spherical harmonics [43]

$$h(t, \theta, \phi, \boldsymbol{\lambda}) = h_+(t, \theta, \phi, \boldsymbol{\lambda}) - i h_\times(t, \theta, \phi, \boldsymbol{\lambda})$$
$$= \sum_{l=2}^{\infty} \sum_{m=-l}^{+l} h^{lm}(t, \boldsymbol{\lambda}) \,_{-2}Y_{lm}(\theta, \phi), \quad (1)$$

where t denotes time, θ and ϕ describe the GW propagation direction, and the symbol $\boldsymbol{\lambda}$ encodes all the binary's intrinsic parameters. For quasi-circular BH binaries, these are the mass ratio q and spin vectors $\boldsymbol{\chi_1}, \boldsymbol{\chi_2}$ (the total mass M is a free scale).

Surrogate models have been presented for both effective-one-body [44–46] and NR waveforms [42, 47]. In this paper we use the NR waveform surrogate model NRSur7dq2 [42] to generate our waveforms. NRSur7dq2 is the very first model able to cover the 7-dimensional parameter space describing generic precessing systems. NRSur7dq2 is trained on 886 NR waveforms generated with the Spectral Einstein Code (SpEC) [48] and interpolated using the technique put forward by [44]. It provides modes h^{lm} up to $l \leq 4$ for binaries with mass ratios $q = m_2/m_1 \in [0.5, 1]$ and dimensionless spin magnitudes $\chi_1, \chi_2 \in [0, 0.8]$; updates to extend its validity range are under active development. The model has been shown to be extremely accurate at reproducing the gravitational-wave strain h: it outperforms all other available waveform approximants by several orders of magnitude, reaching a level of accuracy comparable to the NR simulations used in the training process [42].

Waveforms generated with NRSur7dq2 span the time range $-4500M \leq t \leq 100M$, where $t = 0$ is defined as the time that maximizes the total waveform amplitude $\mathcal{A}^2(t) = \sum_{l,m} |h^{lm}(t)|^2$. The initial time $t = -4500M$ corresponds to about 20 orbits before merger and the final value $t = 100M$ allow for a full dissipation of the signal. Values of h^{lm} are computed at carefully selected time nodes [42] and later interpolated in time using standard cubic univariate B-splines. More specifically, NRSur7dq2 provides the distance-independent dimensionless strain, extrapolated to $\mathcal{I}^+$, i.e. $\lim_{r \to \infty} rh/M$ where r is the distance from the binary's center of mass and M is the total mass of the binary at the beginning of the evolution. NRSur7dq2 allows for the spin directions to be specified at a reference time $-4500M \leq t_{\rm ref} \leq -100M$, in a frame defined such that the more (less) massive BH sits on the positive (negative) x-axis and the Newtonian orbital angular momentum $\mathbf{L}$ lies along the z-axis. Unless otherwise stated, we use $t_{\rm ref} = -100M$.

B. Radiated energy and momenta

Multipolar expansions for the radiated energy, linear momentum and angular momentum have been worked out in detail in [49] (derived from [43, 50]). We report their expressions here for completeness.[1] Whenever terms with $l < 2$ or $|m| > l$ are present in the following summations, their coefficients are intended to be zero. In practice, one is also limited to $l \leq l_{\max}$ (where e.g. $l_{\max} = 4$ for NRSur7dq2 waveforms and $l_{\max} = 8$ for SpEC waveforms).

The energy flux emitted in GWs is provided in terms of the first time derivative of the complex strain $\dot{h}$ and reads:

$$\frac{dE}{dt} = \lim_{r \to \infty} \frac{r^2}{16 \pi} \sum_{l,m} \left| \dot{h}^{l,m} \right|^2 . \quad (2)$$

When integrating to obtain $E(t)$ we set the integration constant E_0 to account for the binding energy dissipated in GWs at times $t < -4500M$, before the start of our waveforms, thus enforcing $\lim_{t \to -\infty} E(t) = 0$. A straightforward Newtonian (0PN) calculation yields [52]

$$\frac{E_0}{M} = \left(\frac{5}{1024} \frac{q^3}{(1+q)^6} \dot{E}_0 \right)^{1/5}, \quad (3)$$

where $\dot{E}_0$ is estimated from Eq. (2) by averaging over the first $100M$ in time. We have verified that corrections up to 2PN (including spin effects [53]) have a negligible

---

[1] Ref. [43] presents his formulas in specially-chosen coordinate systems. A more rigorous mathematical framework for these calculations is to go to $\mathcal{I}^+$ and present the news tensor, Bondi mass aspect, and other Bondi charges (e.g. [51]). Ref. [49] uses the convention $\text{Im}(a + ib) = ib$ while here we use $\text{Im}(a + ib) = b$.

impact on E_0. One can then define the time-dependent (Bondi) mass of the binary,

$$M(t) = M - E(t) + E_0 \,, \qquad (4)$$

such that $M(t)$ at the beginning of our waveforms is equal to M. The mass of the post-merger BH in units of the total mass of the binary at early times is

$$\frac{\lim_{t \to +\infty} M(t)}{\lim_{t \to -\infty} M(t)} = 1 - \frac{\lim_{t \to +\infty} E(t)}{M + E_0} \,. \qquad (5)$$

The emitted linear momentum is also fully specified by $\dot{h}$ and crucially includes mixing between modes with different l and m:

$$\frac{dP_x}{dt} = \lim_{r \to \infty} \frac{r^2}{8\,\pi} \, \mathrm{Re} \left[\sum_{l,m} \dot{h}^{l,m} \Big(a_{l,m}\, \dot{\bar{h}}^{l,m+1} \right.$$
$$\left. + b_{l,-m}\, \dot{\bar{h}}^{l-1,m+1} - b_{l+1,m+1}\, \dot{\bar{h}}^{l+1,m+1} \Big) \right] \,, \quad (6)$$

$$\frac{dP_y}{dt} = \lim_{r \to \infty} \frac{r^2}{8\,\pi} \, \mathrm{Im} \left[\sum_{l,m} \dot{h}^{l,m} \Big(a_{l,m}\, \dot{\bar{h}}^{l,m+1} \right.$$
$$\left. + b_{l,-m}\, \dot{\bar{h}}^{l-1,m+1} - b_{l+1,m+1}\, \dot{\bar{h}}^{l+1,m+1} \Big) \right] \,, \quad (7)$$

$$\frac{dP_z}{dt} = \lim_{r \to \infty} \frac{r^2}{16\pi} \sum_{l,m} \dot{h}^{l,m} \Big(c_{l,m}\, \dot{\bar{h}}^{l,m}$$
$$+ d_{l,m}\, \dot{\bar{h}}^{l-1,m} + d_{l+1,m}\, \dot{\bar{h}}^{l+1,m} \Big) \,, \qquad (8)$$

where the upper bar denotes complex conjugation and

$$a_{l,m} = \frac{\sqrt{(l-m)\,(l+m+1)}}{l\,(l+1)} \,, \qquad (9)$$

$$b_{l,m} = \frac{1}{2\,l} \sqrt{\frac{(l-2)\,(l+2)\,(l+m)\,(l+m-1)}{(2l-1)(2l+1)}} \,, \quad (10)$$

$$c_{l,m} = \frac{2\,m}{l\,(l+1)} \,, \qquad (11)$$

$$d_{l,m} = \frac{1}{l} \sqrt{\frac{(l-2)\,(l+2)\,(l-m)\,(l+m)}{(2l-1)(2l+1)}} \,. \qquad (12)$$

The integration constant for the $d\mathbf{P}/dt$ integration is chosen so that the average of $\mathbf{P}$ over the first $1000M$ in time, where linear momentum emission is expected to be negligible, is zero. By conservation of linear momentum, the time profile of the kick imparted to the system is[2]

$$\mathbf{v}(t) = -\frac{P_x(t)\hat{\mathbf{x}} + P_y(t)\hat{\mathbf{y}} + P_z(t)\hat{\mathbf{z}}}{M(t)} \,, \qquad (13)$$

---

[2] Relativistic corrections are irrelevant here. The largest BH kicks are $v_k/c \sim 10^{-2}$ corresponding to Lorentz factors $\gamma - 1 \sim 10^{-4}$.

and the final velocity of the post-merger remnant BH is

$$\mathbf{v_k} = \lim_{t \to \infty} \mathbf{v}(t) \,. \qquad (14)$$

One can further integrate $\mathbf{v}(t)$ in time to obtain the trajectory $\mathbf{x}(t) = \int \mathbf{v}(t)dt$. Although the binary trajectory is a coordinate-dependent notion, the time integral of the linear momentum dissipated in GWs can be interpreted as the motion of the spacetime's center of mass seen by an observer at $\mathcal{I}^+$ [51].

The angular momentum carried by GWs involves both h and $\dot{h}$:

$$\frac{dJ_x}{dt} = \lim_{r \to \infty} \frac{r^2}{32\pi} \, \mathrm{Im} \left[\sum_{l,m} h^{l,m} \Big(f_{l,m}\, \dot{\bar{h}}^{l,m+1} \right.$$
$$\left. + f_{l,-m}\, \dot{\bar{h}}^{l,m-1} \Big) \right] \,, \qquad (15)$$

$$\frac{dJ_y}{dt} = -\lim_{r \to \infty} \frac{r^2}{32\pi} \, \mathrm{Re} \left[\sum_{l,m} h^{l,m} \Big(f_{l,m}\, \dot{\bar{h}}^{l,m+1} \right.$$
$$\left. - f_{l,-m}\, \dot{\bar{h}}^{l,m-1} \Big) \right] \,, \qquad (16)$$

$$\frac{dJ_z}{dt} = \lim_{r \to \infty} \frac{r^2}{16\pi} \, \mathrm{Im} \left[\sum_{l,m} m\, h^{l,m}\, \dot{\bar{h}}^{l,m} \right] \,, \qquad (17)$$

where

$$f_{l,m} = \sqrt{l(l+1) - m(m+1)} \,. \qquad (18)$$

When integrating $d\mathbf{J}/dt$, we do not adjust the integration constant to account for the angular momentum radiated before the beginning of our waveforms. Contrary to the binding energy, the Newtonian angular momentum of a binary system diverges as separation grows ($J \propto \sqrt{r}$).

We perform all differentiations and integrations required to extract these radiated quantities analytically on the spline interpolants provided by NRSur7dq2, over the range $-4500M \le t \le 100M$. The $t \to \infty$ limits [e.g. Eqs. (5) and (14)] are approximated with values at $t = 100M$.

III. RESULTS

A. Anatomy of the kick

Non-spinning BH binaries do not receive any recoil for both $q = 1$ (because of symmetry) and $q = 0$ (which corresponds to the test-particle limit). Recoils are present in between these two limits. Fig. 1 shows the kick profile $\mathbf{v}(t)$ for a series of BH mergers with $q = 0.5, \dots, 1$. Axisymmetry prevents linear momentum dissipation along the direction of the orbital angular momentum, i.e. $\mathbf{v}(t) \cdot \hat{\mathbf{z}} = 0$ (within numerical errors, see Sec. IV A). The binary's center of mass oscillates in the orbital plane xy during

the inspiral, until the merger halts these oscillations and imparts the final recoil. The kick velocity grows as q decreases, reaching $v_k \simeq 148$ km/s for $q = 0.5$. The largest kick achievable for non-spinning system is $v_k \simeq 175$ km/s and corresponds to $q \sim 0.36$ [37], which is outside the parameter space currently covered by NRSur7dq2. The trajectory of the spacetime's center of mass $\mathbf{x}(t)$ for $q = 0.5$ and $\chi_1 = \chi_2 = 0$ is shown in the left panel of Fig. 2. One last oscillation occurs after merger, and is responsible for most of the kick. This effect is also visible in Fig. 1, where we see the system typically accelerates at $t \sim 10M$ after merger, with the final burst of linear momentum radiation lasting only for a few M in time. Interestingly, the projection of the recoil profile along the final kick direction $\mathbf{v}(t) \cdot \hat{\mathbf{v}}_{\mathbf{k}}$ is not monotonic after merger: the binary suddenly decelerates at about $t \sim 15M$, after which the imparted velocity settles down to the asymptotic value v_k. This effect has been dubbed *antikick* [54], and turns out to be a rather generic feature of BH mergers (c.f. Sec. III B below).

BH spins introduce additional sources of linear momentum dissipation. The impact of aligned spins on the radiated energy and linear momentum profile is illustrated in Fig. 3 and 4, respectively. In particular, we study BH binaries with spin magnitude $\chi_1 = \chi_2 = 0.8$ and four different spin orientations: $\hat{\boldsymbol{\chi}}_{\mathbf{1}} \cdot \hat{\mathbf{z}} = \hat{\boldsymbol{\chi}}_{\mathbf{2}} \cdot \hat{\mathbf{z}} = 1$ (up-up), $\hat{\boldsymbol{\chi}}_{\mathbf{1}} \cdot \hat{\mathbf{z}} = \hat{\boldsymbol{\chi}}_{\mathbf{2}} \cdot \hat{\mathbf{z}} = -1$ (down-down), $\hat{\boldsymbol{\chi}}_{\mathbf{1}} \cdot \hat{\mathbf{z}} = -\hat{\boldsymbol{\chi}}_{\mathbf{2}} \cdot \hat{\mathbf{z}} = 1$ (up-down), $\hat{\boldsymbol{\chi}}_{\mathbf{1}} \cdot \hat{\mathbf{z}} = -\hat{\boldsymbol{\chi}}_{\mathbf{2}} \cdot \hat{\mathbf{z}} = -1$ (down-up), where $\hat{\mathbf{z}} = \hat{\mathbf{L}}$ at $t_{\rm ref} = -100M$. Although the up-down configuration is generically unstable to spin precession [55], the instability develops on longer timescales and can therefore be neglected in this context. The orbital hang-up effect [56–58] causes binaries with spins co- (counter-) aligned with the binary's angular momentum to merge later (sooner) compared to non-spinning systems with the same mass ratio. Consequently, the energy emitted in GWs increases (decreases) if the total spin $\mathbf{S} = m_1^2 \boldsymbol{\chi}_{\mathbf{1}} + m_2^2 \boldsymbol{\chi}_{\mathbf{2}}$ is (anti-)aligned with $\mathbf{L}$ (c.f. Fig. 3). For $q = 1$ (Fig. 4, left panel), moderately large recoils of $v_k \sim 350$ km/s are achieved for the up-down and down-up configurations, in agreement with the PN predictions $v_k \propto |\hat{\boldsymbol{\chi}}_{\mathbf{1}} \cdot \hat{\mathbf{L}} - \hat{\boldsymbol{\chi}}_{\mathbf{2}} \cdot \hat{\mathbf{L}}|$ [6] (see [38, 59] for numerical explorations). The recoil is mostly imparted in the orbital plane, but its magnitude is somewhat smaller than the mass-asymmetry case explored above and reduces to a single burst of linear momentum emitted at $t \sim 10M$, preceded by a smaller one in the opposite direction at $t \sim -5M$. The $q = 1$ up-up configuration presents some linear momentum emitted perpendicular to the orbital plane, resulting in $v_k \sim 50$ km/s. This is the inherent error scale in our model, as symmetry implies $v_k = 0$ for both the up-up and down-down configuration at $q = 1$ [60, 61], see Sec. IV A. For binaries with unequal masses and aligned spins (Fig. 4, right panel), both the orbital hang-up and the mass asymmetry effect are present: the binary's center of mass first oscillates in the orbital plane (because $q \neq 1$) and then receive a further push at $t \sim 10M$ (because $\boldsymbol{\chi_i} \cdot \hat{\mathbf{z}} \neq 0$).

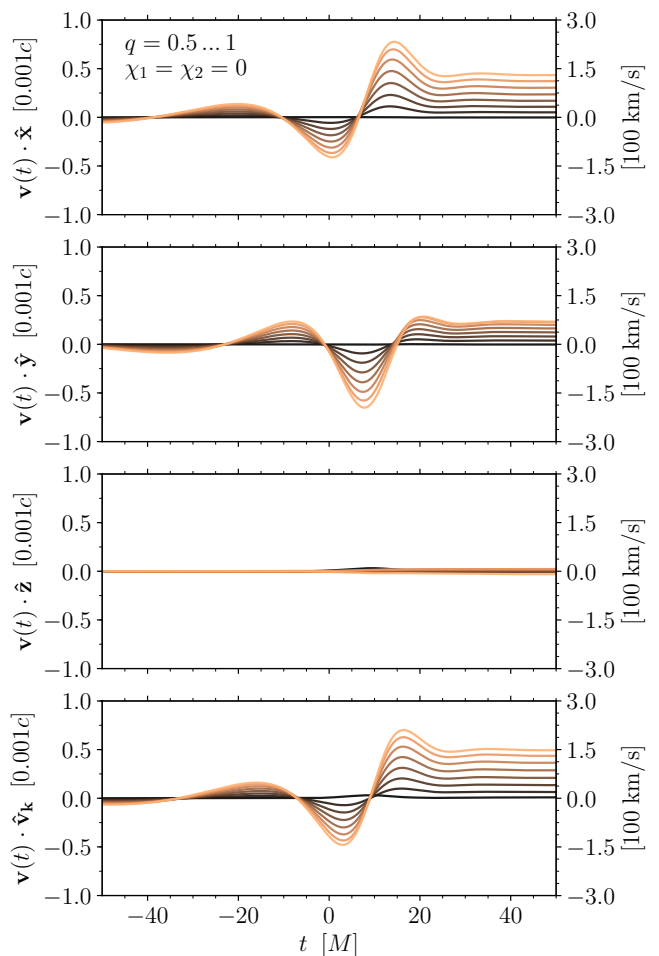The largest kicks are achieved for BHs merging with

FIG. 1. Kick profile $\mathbf{v}(t)$ projected along $\hat{\mathbf{x}}$, $\hat{\mathbf{y}}$, $\hat{\mathbf{z}}$ and the direction of the final kick $\hat{\mathbf{v}}_{\mathbf{k}}$ for a series of non-spinning BH binaries with mass ratio ranging from $q = 0.5$ (light orange) to $q = 1$ (black). The binary's center of mass oscillates in the orbital plane during the inspiral; the final recoil is imparted with a sudden acceleration at $t \sim 10M$ after the peak-amplitude time.

misaligned spins [11–14, 36, 41]. Fig. 5 shows kick profiles for four binary configurations with spins $\chi_i = 0.8$ lying in the orbital plane: $\hat{\boldsymbol{\chi}}_{\mathbf{1}} \cdot \hat{\mathbf{x}} = \hat{\boldsymbol{\chi}}_{\mathbf{2}} \cdot \hat{\mathbf{x}} = 1$ (right-right), $\hat{\boldsymbol{\chi}}_{\mathbf{1}} \cdot \hat{\mathbf{x}} = \hat{\boldsymbol{\chi}}_{\mathbf{2}} \cdot \hat{\mathbf{x}} = -1$ (left-left), $\hat{\boldsymbol{\chi}}_{\mathbf{1}} \cdot \hat{\mathbf{x}} = -\hat{\boldsymbol{\chi}}_{\mathbf{2}} \cdot \hat{\mathbf{x}} = 1$ (right-left), $\hat{\boldsymbol{\chi}}_{\mathbf{1}} \cdot \hat{\mathbf{x}} = -\hat{\boldsymbol{\chi}}_{\mathbf{2}} \cdot \hat{\mathbf{x}} = -1$ (left-right), where $\hat{\mathbf{x}}$ is defined as the axis connecting the lighter to the heavier BH at $t_{\rm ref}$. For reasons clarified below, here we take $t_{\rm ref} = -125M$. Kicks as large as ~ 2820 km/s are achieved for the right-left and left-right configurations, which correspond to the *superkick* scenario discovered by [11, 12]. During the inspiral, frame dragging from the two holes acts constructively and pushes the binary's center of mass up and down along the direction of the orbital angular momentum $\hat{\mathbf{z}}$. The final kick is imparted as the BHs merge and the last of these oscillations is abruptly interrupted. The phenomenology is rather similar to the case of aligned spins studied above, although with
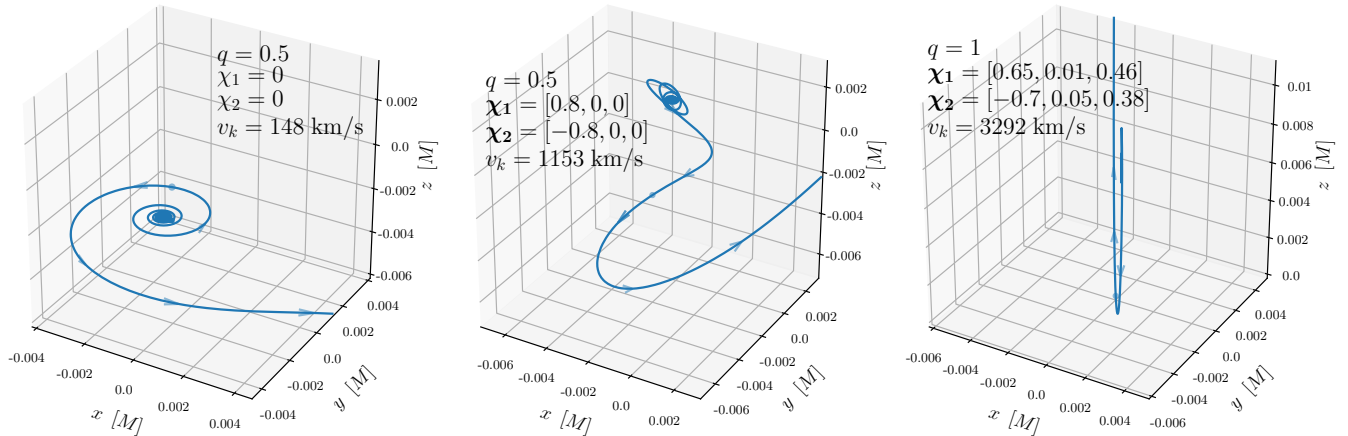
FIG. 2. Center of mass trajectory $\mathbf{x}(t) = \int \mathbf{v}(t)dt$ for three binary configurations as described in the legends. The circle markers on each curve correspond to $t = 0$. The left panel shows a recoil due to mass asymmetry only: the center of mass oscillates in the orbital plane during the inspiral and is finally pushed after merger. The middle panel shows a complicated interplay of mass and spin asymmetry, with the initial oscillations being greatly distorted at merger by the superkick effect. Finally, the right panel shows the simpler trajectory of a binary receiving a very large kick of ~ 3000 km/s. An animated version of this figure is available at davidegerosa.com/surrkick.
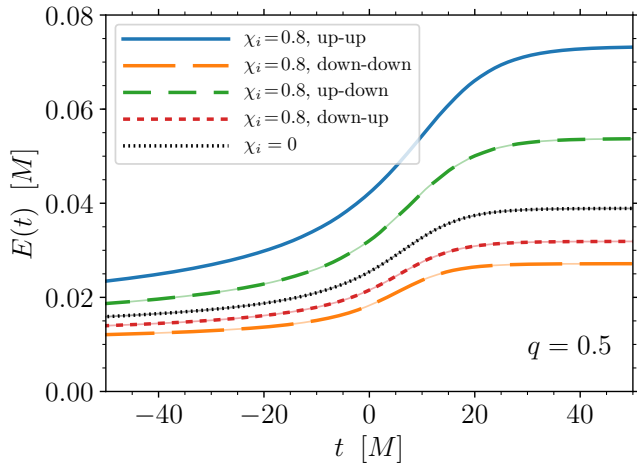
FIG. 3. Radiated energy $E(t)$ for binaries with mass ratio $q = 0.5$ and spins of magnitude $\chi_1 = \chi_2 = 0.8$ (anti)aligned to the orbital angular momentum. Four configurations are shown: up-up, down-down, up-down, down-up, where the term before (after) the hyphen refers to the spin of the heavier (lighter) BH being co-/counter-aligned with the binary's orbital angular momentum. For comparison, we also show $E(t)$ for a non-spinning system with the same mass ratio. Because of the orbital hang-up effect, BH binaries with (anti-)aligned spins radiate more (less) energy compared to non-spinning systems with the same mass ratio.

the key difference that in this case linear momentum is emitted along the binary's orbital angular momentum, not orthogonal to it. It is worth noting that binaries with these large kicks present a remarkably simple accumulation profile: the acceleration $d\mathbf{P}/dt$ is well described by a

Gaussian centered at $t \sim 10M$ with width $\sigma \sim 5M$ (c.f. [41] and Sec. III B below). Conversely, frame dragging from the two BHs add destructively for the right-right and left-left binaries. This cancellation is perfect (within numerical errors, c.f. Sec. IV A) if the two spins have the same magnitude $m_1^2\chi_1 = m_2^2\chi_2$ (Fig. 5, left panel). For $q = 0.5$ and $\chi_i = 0.8$ (Fig. 5, right panel), the dynamics is dominated by the largest spin and the four configurations reach values between 650 and 1530 km/s. Interestingly, smaller mass ratios excite a sizable kick along the orbital plane of ~ 300 km/s, which exceed the recoil imparted to non-spinning systems with the same q of about a factor ~ 2 (c.f. Fig. 1). The spacetime trajectory $\int \mathbf{v}(t)dt$ for one of such binaries is illustrated in the middle panel of Fig. 2: the center of mass oscillates at early time, undergoes a complicated motion right before merger, after which the superkick effect starts dominating. To the best of our knowledge, this mass-spin asymmetry mixing in the kick profile has not been reported elsewhere.

Superkick velocities critically depend on the orbital phase at merger, as it controls the abrupt interruption of the oscillatory behavior described above. In the left panel of Fig. 6 we study a series of right-left binaries ($q = 1$, $\chi_1 = \chi_2 = 0.8$, $\hat{\boldsymbol{\chi}}_1 \cdot \hat{\mathbf{x}} = -\hat{\boldsymbol{\chi}}_2 \cdot \hat{\mathbf{x}} = 1$) specified at various reference times $t_{\mathrm{ref}}/M \in [-250, -100]$. The final kick velocity v_k shows a clear sinusoidal dependence, as already found by e.g. [39, 41, 62]. The peaks (e.g. at $t \sim -125M$) correspond to configurations for which the center of mass velocity happens to be at its maximum when the last oscillation is interrupted. The orbital phase at merger can also be controlled by an overall rotation of both spins about the orbital angular momentum. The right panel of Fig. 6 shows v_k for binaries with spins $\hat{\boldsymbol{\chi}}_1 = -\hat{\boldsymbol{\chi}}_2 = [\cos\alpha, \sin\alpha, 0]$ specified at $t_{\mathrm{ref}} = -100M$
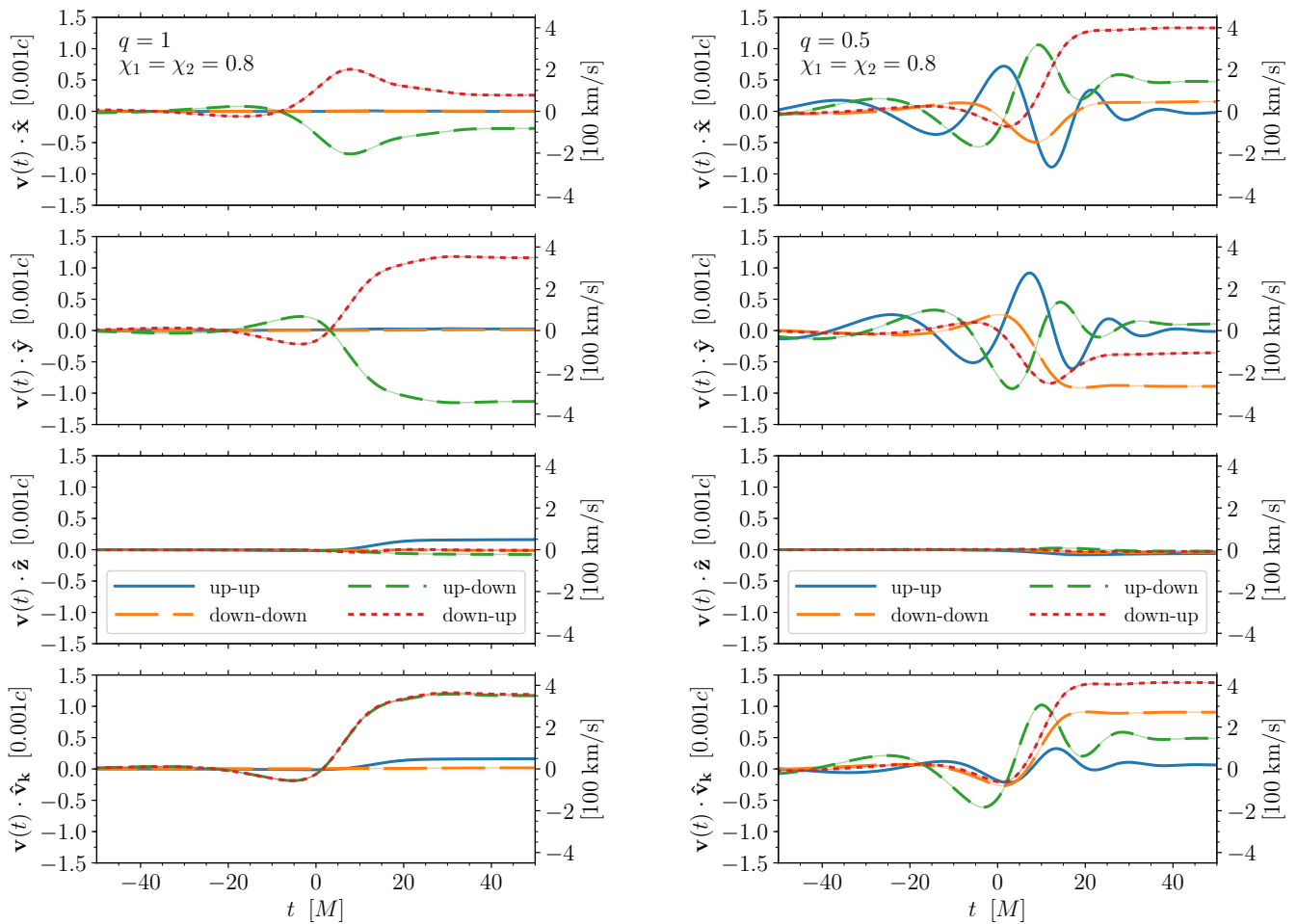
FIG. 4. Kick profile $\mathbf{v}(t)$ projected along $\hat{\mathbf{x}}$, $\hat{\mathbf{y}}$, $\hat{\mathbf{z}}$ and the direction of the final kick $\hat{\mathbf{v}}_{\mathbf{k}}$ for binaries with mass ratio $q = 1$ (left) and $q = 0.5$ (right), and spins of magnitude $\chi_1 = \chi_2 = 0.8$ (anti)aligned to the orbital angular momentum. Four configurations are shown: up-up, down-down, up-down, down-up, where the term before (after) the hyphen refers to the spin of the heavier (lighter) BH being co-/counter-aligned with the binary's orbital angular momentum. Kicks from non-precessing systems lie in the binary's orbital plane, with the spin kicks being more pronounced for the up-down and down-up configurations in accordance with PN predictions.

(a similar series of NR simulations was reported in [41]). The right-left (left-right) configuration corresponds to $\alpha = 0$ (π). The two curves in Fig. 6 span the very same range, showing that the angle α and the reference time t_{ref} are indeed degenerate. In practice, this means that only binaries with a specific orbital phase at merger are subject to superkicks, thus making their occurrence very rare. Fig. 7 shows the velocity accumulation profile for the same series of binaries with different values of α: the BH merger abruptly stops the center-of-mass oscillation at different phases, thus setting the final kick velocities.

As first noted in [14, 40], binaries with partially aligned spins give rise to BH kicks even larger than those imparted to binaries in the superkick configuration. Equal-mass, maximally spinning BH binaries are predicted to reach $v_k \sim 5000$ km/s for spins misaligned by angles $\theta_i = \cos^{-1}(\hat{\boldsymbol{\chi}}_i \cdot \mathbf{L}) \sim 50°$. These recoils were dubbed *hang-up kicks*, and are due to a combination of the BH frame

dragging addition (responsible for superkicks) and the orbital hang-up effect (which enhances the energy radiated in GWs for aligned spins). To check that our model reproduces these hang-up kicks, we generate 10^5 binaries with $q = 1$, $\chi_1 = \chi_2 = 0.8$, and isotropic spin orientations. The largest kick detected is $v_k \sim 3300$ km/s, and is obtained for $\theta_1 \sim \theta_2 \sim 57°$. For the same values q, χ_1 and χ_2, the hang-up kick fitting formula of [14, 40] returns a largest kick of ~ 3500 km/s (a more careful comparison is postponed to Sec. III B). The spacetime trajectory corresponding to one of these cases is shown in the right panel of Fig. 2, confirming our earlier claims that large kicks present rather simple accumulation profiles.

Finally, Fig. 8 explores projection effects of the kick accumulation profile. For a single system with $q = 0.5$ and $\chi_1 = \chi_2 = 0.8$ in the right-left configuration, we show the projection of $\mathbf{v}(t)$ along various randomly chosen directions $\hat{\mathbf{n}}$. Although some features are solid, the kick
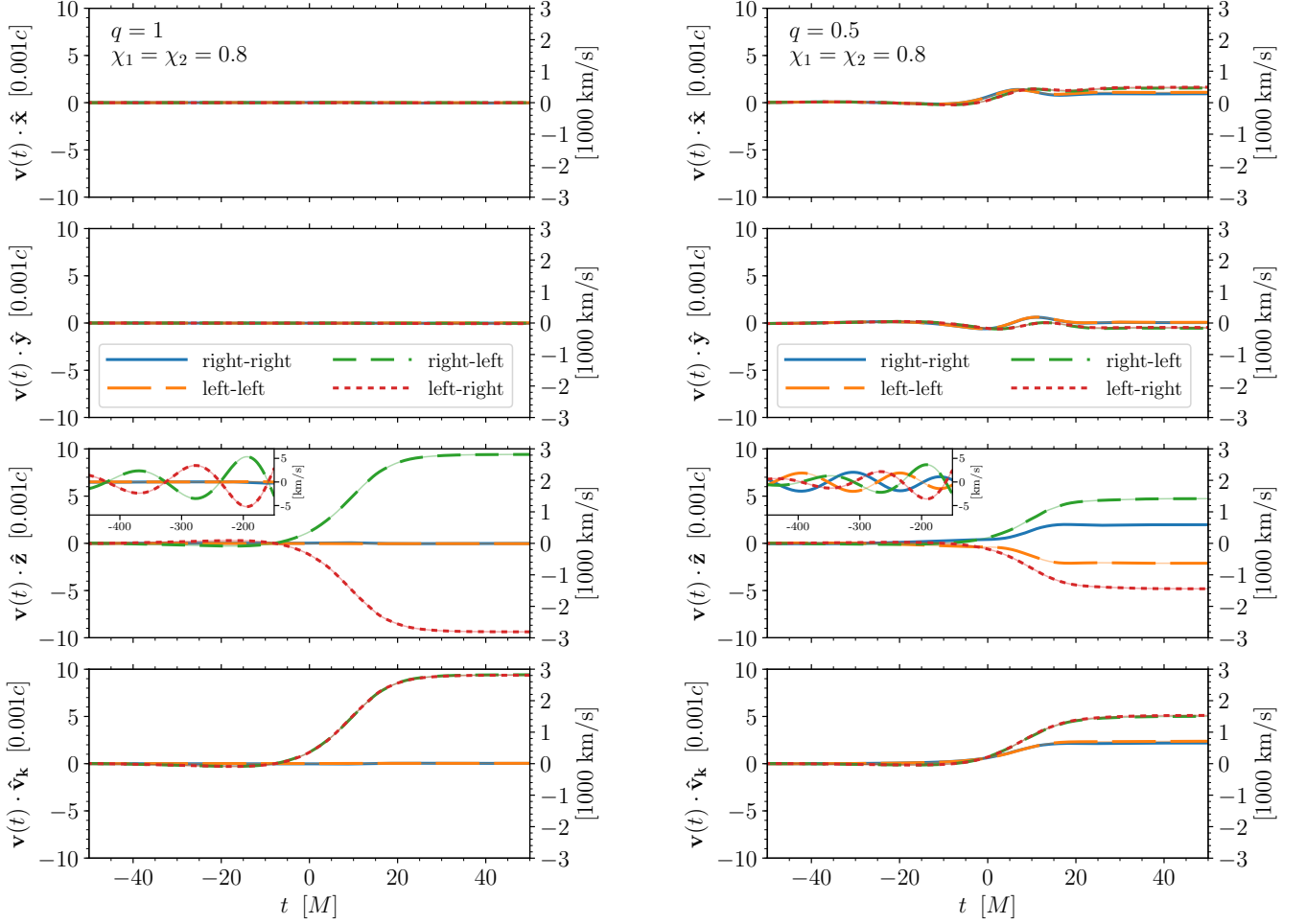
FIG. 5. Kick profile $\mathbf{v}(t)$ projected along $\hat{\mathbf{x}}$, $\hat{\mathbf{y}}$, $\hat{\mathbf{z}}$ and the direction of the final kick $\hat{\mathbf{v}}_{\mathbf{k}}$ for binaries $q = 1$ (left) and $q = 0.5$ (right), and spins of magnitude $\chi_1 = \chi_2 = 0.8$ lying into the orbital plane. Four configurations are shown: right-right, left-left, right-left, left-right, where the term before (after) the hyphen refers to the spin of the heavier (lighter) BH being co-/counter-aligned with initial separation vector $\hat{\mathbf{x}}$. The right-left and left-right orientations correspond to the superkick configurations. Here we set $t_{\rm ref} = -125M$ to maximize kicks for the $q = 1$ case (c.f. Fig. 6).
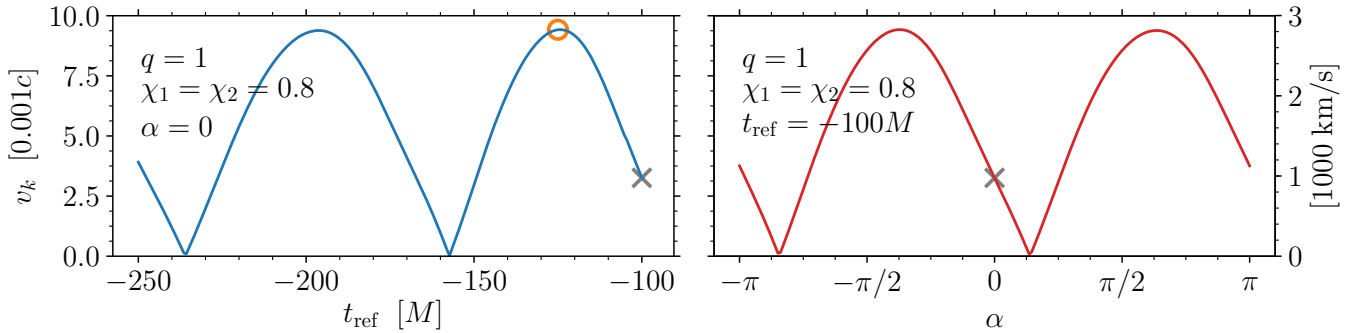
FIG. 6. Left panel: Recoil velocities for a series of right-left binaries with $q = 1$ and $\chi_i = 0.8$ initialized at various reference times $t_{\rm ref}$; the orange circle marks the reference time used in Fig. 5. Right panel: Recoil velocities for BH binaries with $q = 1$ and $\boldsymbol{\chi_1} = -\boldsymbol{\chi_2} = [0.8\cos\alpha, 0.8\sin\alpha, 0]$ (such that $\alpha = 0$ corresponds to the right-left configuration) at $t_{\rm ref} = -100M$. The angle α corresponds to a rotation of both spins about the orbital angular momentum, and is degenerate with the reference time at which spins are specified. Gray crosses mark the same configuration in both panels.
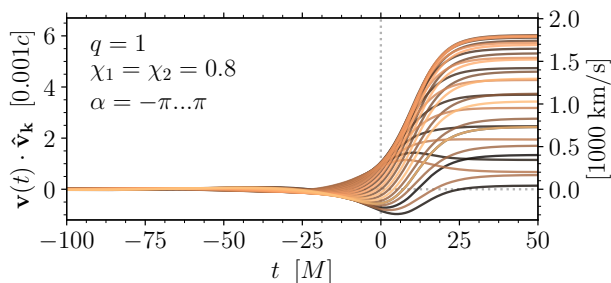
FIG. 7. Velocity accumulation profile $\mathbf{v}(t)$ projected along the direction of the final kick $\hat{\mathbf{v}}_{\mathbf{k}}$ for binaries with $q = 1$ and anti-parallel spins of magnitude $\chi_1 = \chi_2 = 0.8$ lying in the orbital plane. The rotation angle α (defined as $\cos \alpha = \hat{\boldsymbol{\chi}}_1 \cdot \hat{\mathbf{x}} = -\hat{\boldsymbol{\chi}}_2 \cdot \hat{\mathbf{x}}$) controls the orbital phase at merger and thus sets the velocity of the center of mass when the final kick is imparted. Curves are colored according to α as it spans from $-\pi$ (black) to π (orange).
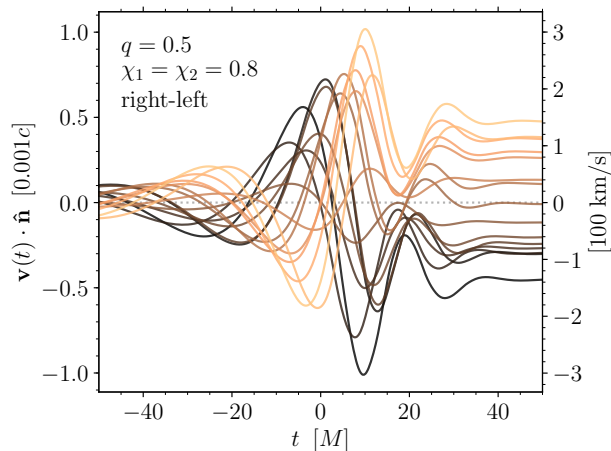
FIG. 8. Kick profiles for a right-left binary with $q = 0.5$ and $\chi_1 = \chi_2 = 0.8$ projected along various random directions $\hat{\mathbf{n}}$. Curves are colored from black to orange according to the final projected kick $\lim_{t \to \infty} \mathbf{v}(t) \cdot \hat{\mathbf{n}}$.

profile appears rather differently if viewed from different orientations. This behavior is important to model BHs recoiling into astrophysical environments with well defined geometries, such as accretion disks [63, 64], and to implement the effect of the BH kick in waveform models through the induced Doppler shift [35].

B. Statistical exploration and comparison with fitting formulae

After exploring the main features of the kick profile in controlled scenarios, we now turn our attention to statistical samples. We generate a sample of 10^6 binaries with mass ratio uniform in $q \in [0.5, 1]$ and spins uniformly distributed in volume with magnitude $\chi_i \leq 0.8$. Fig. 9 shows the distributions of total energy, linear momentum, and

angular momentum radiated in GWs by this BH binary population. The energy and angular momentum distributions are roughly symmetric, with peaks at $E \sim 0.045M$ and $J \sim 0.45M^2$, respectively. The recoil distribution peaks at $v_k \sim 0.001c$, with a long tail extending up to $v_k \sim 0.01c \sim 3000$ km/s. Fig. 9 also shows predictions for v_k obtained with fitting formulae currently available in the literature. In particular, we use the expressions summarized in [65], which are calibrated on various numerical simulations by [36–40]. Although kick predictions for individual binaries might differ significantly, the two methods largely agree on the overall distribution. We note, however, that the fitting formula tends to overestimate the number of binaries receiving large recoils. In particular, the fractions of binaries with $v_k > 2000$ km/s are $\sim 2.4\%$ and $\sim 3.2\%$ for surrogate extraction and fitting formula, respectively. The largest kicks found in these distributions are $v_k \sim 3160$ km/s (surrogate) and $v_k \sim 3330$ km/s (fit). We speculate this disagreement might be due to the calibration of the hang-up kick terms in the fitting formula, which was only performed with $q = 1$ simulations (c.f. [66] for a critical discussion on this point). Although some runs for unequal-mass binaries with largely misaligned spins have been presented [36, 62, 67, 68], the effect of the mass ratio on the largest kick might not be fully captured by the expressions currently available. Fig. 9 also compares the total radiated energy extracted from the surrogate model against the final-mass fitting formula of [69], corrected according to Eq. (5). Agreement is found at the $\sim 2\%$ level: the median for the surrogate (fit) estimate of E/M is ~ 0.047 (~ 0.046) with standard deviations of ~ 0.008 (~ 0.009). Ref. [70] presented a careful analysis comparing different estimates of the energy radiated following BH mergers and reported similar, if not higher, differences between various approaches.

In order to highlight the "shape" of the kick, Fig. 10 shows 200 velocity accumulation profiles $\mathbf{v}(t)$ from the same binary distribution projected along random directions $\hat{\mathbf{n}}$ and normalized to the value of the final kick $\mathbf{v}_{\mathbf{k}} \cdot \hat{\mathbf{n}}$. Despite the remarkable complexity explored above, the kick accumulation profiles present very robust features. In particular, profiles are simpler for binaries receiving large recoils, for which the acceleration $d\mathbf{v}/dt \cdot \hat{\mathbf{n}}$ is well approximated by a single Gaussian with mean $t = 10M$ and width $\sigma = 8M$. Smaller kicks, on the other hand, present more complicated profiles which typically include an antikick [54]. These findings corroborate the approach of [35], where $\mathbf{v}(t) \cdot \hat{\mathbf{n}}$ is modeled with a basis of damped oscillatory functions.

We stress that the population explored here are far from being astrophysically relevant. Astrophysical processes (such as the Bardeen-Petterson effect in case of disk accretion [71] and tidal interactions for stellar-mass BH progenitors [72]) deeply modify the BH spin orientations, thus affecting the expected kick distribution [73–75]. Moreover, PN effects in the long inspiral before merger have been shown to preferentially suppress or enhance recoils in specific regions of the parameter space [75, 76].
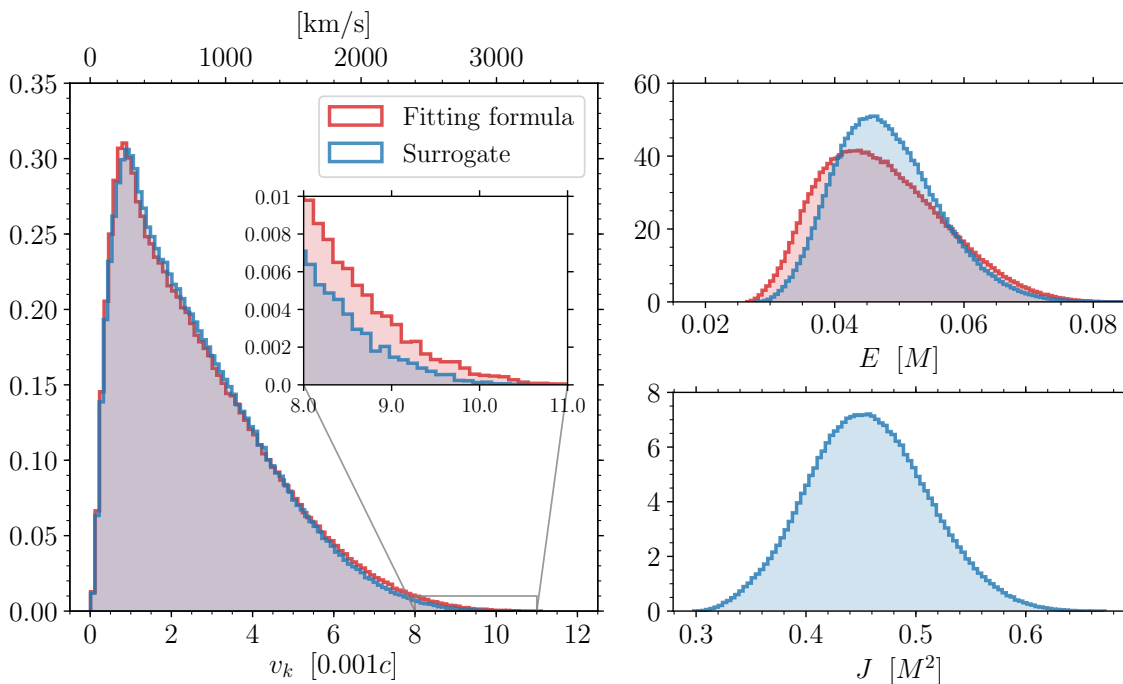
FIG. 9. Distribution of radiated linear momentum v_k (left panel), energy E (top right panel) and angular momentum J (bottom right panel) for a distribution of binaries with mass ratio uniformly distributed in $[0.5, 1]$ and spin of magnitude $\chi_i < 0.8$ uniformly distributed in volume. Our results ("Surrogate") are compared to the model summarized in [65] based on [36–40] ("Fitting formula"): the two distributions largely agree, although differences are present for large values of v_k.
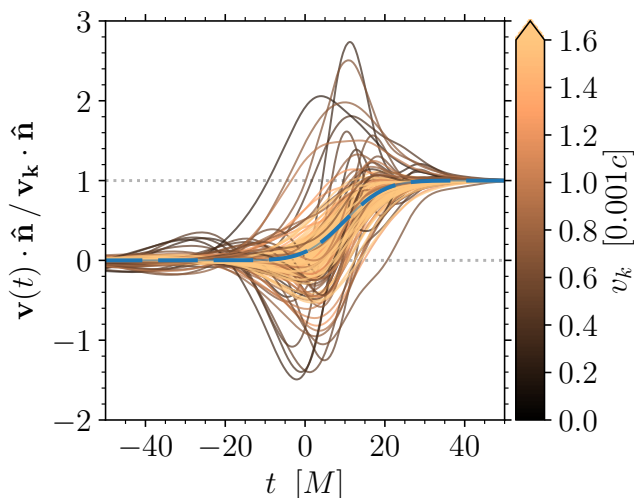

FIG. 10. Kick profiles $\mathbf{v}(t)$ for a sample of BH binaries with uniform mass ratio and isotropic spin directions projected along random directions $\hat{\mathbf{n}}$. Curves are normalized according to the final projected kick $\mathbf{v_k} \cdot \hat{\mathbf{n}}$ and are colored according to the total kick magnitude v_k. The dashed blue line corresponds to a Gaussian acceleration profile of width $\sigma = 8M$ centered at $t = 10M$, which well approximates the largest kick in our sample. Smaller kicks require more complicated profiles to be modeled carefully.

IV. ACCURACY

A. Exploiting symmetries

Before presenting a detailed comparison with NR simulations, we first perform internal tests of our kick extraction procedure by leveraging the symmetries of the problem. For instance, equal mass nonspinning systems are not expected to recoil ($v_k = 0$). Our extraction procedure returns $v_k \sim 10^{-5}$, which has to be considered a numerical error. Following [60, 61], we further exploit this argument using other symmetries of the system. In particular:

(i) $q = 1$ and $\boldsymbol{\chi_1} = \boldsymbol{\chi_2}$ imply $v_k = 0$;

(ii) aligned spins ($\boldsymbol{\chi_1} \parallel \hat{\mathbf{L}}$ and $\boldsymbol{\chi_2} \parallel \hat{\mathbf{L}}$) force the recoil to be confined to the orbital plane ($\mathbf{v_k} \cdot \hat{\mathbf{L}} = 0$); this property is independent of q;

(iii) for $q = 1$ and spins with opposite orbital-plane components ($\boldsymbol{\chi_1} \cdot \hat{\mathbf{L}} = \boldsymbol{\chi_2} \cdot \hat{\mathbf{L}}$ and $\boldsymbol{\chi_1} \times \hat{\mathbf{L}} = -\boldsymbol{\chi_2} \times \hat{\mathbf{L}}$) the kick is restricted to be orthogonal to the orbital plane ($\mathbf{v_k} \parallel \hat{\mathbf{L}}$).

Some of the special cases encountered in Sec. III A belong to these classes. For instance, equal-mass non-spinning systems are a trivial example of all categories. The $q = 1$ up-up, down-down, right-right and left-left cases shown

in Figs. 4 and 5 are an instance of (i) and are therefore expected to have $v_k = 0$. All up-up, down-down, up-down and down-up configurations are an instance of (ii), while right-left and left-right binary with $q = 1$ are an instance of (iii).

These symmetries are investigated in the three panels of Fig. 11, respectively. For the top panel, we generate binaries with $q = 1$ and random spins $\chi_1 = \chi_2$ uniform in volume with magnitude < 0.8. For the middle panel, we take q to be uniformly distributed in $[0.5, 1]$, generate $\chi_i \cdot \hat{z}$ uniformly in $[-0.8, 0.8]$, and set all the x and y components of the spins to zero. For the bottom panel, we fix $q = 1$, generate χ_1 uniform in volume with magnitude < 0.8, and set $[\chi_{2x}, \chi_{2y}, \chi_{2z}] = [-\chi_{1x}, -\chi_{1y}, \chi_{1z}]$. The values of v_k, $|\mathbf{v_k} \cdot \hat{z}|$ and $|\mathbf{v_k} \times \hat{z}|$ shown in Fig. 11 are expected to be zero under symmetries (i), (ii) and (iii), respectively. We see that symmetry (i) exhibits the largest violations. The absolute largest deviations are $\sim 6 \times 10^{-4}c \sim 180$ km/s, which is therefore a generous upper limit of our numerical errors. The median of the errors is as small as $\sim 1.1 \times 10^{-4}c$, while the 90th percentile is $\sim 2.8 \times 10^{-4}c$. Symmetries (ii) and (iii) are better preserved, with a precision which is roughly an order of magnitude higher. The error medians for both are $\sim 1.5 \times 10^{-5}c$.

It is worth noting that the errors reported here are rather conservative, as they take into account inaccuracies accumulated throughout the entire extraction pipeline—from the NR simulations that were used to calibrate NRSur7dq2, to the surrogate waveform interpolations, and finally the numerical operations described in this paper.

B. Comparison with numerical relativity simulations: SpEC.

We now estimate the accuracy of our extraction procedure by directly comparing our results to numerical relativity simulations from the SpEC code [48]. In particular, we compare against the 744 simulations[3] used to construct NRSur7dq2 [42]. These simulations constitute the majority of the waveforms available in the SpEC catalog [77] in the relevant parameter range, and especially so for generic spin orientations. This is not the most ideal comparison: each of these numerical simulation occupies a special point in the binary parameter space of the surrogate model. However, it is worth noting that (i) the surrogate waveforms do not reproduce the NR waveforms exactly, even at the parameter-space location of the simulations that entered the training process; and (ii) NRSur7dq2 was designed to maximize the

---

[3] NRSur7dq2 is trained on 886 waveforms obtained from 744 simulations — 142 simulations have $q = 1$ and $\chi_1 \neq \chi_2$, so that a rotation enables one simulation to represent two sets of binary parameters and therefore two input waveforms [42].
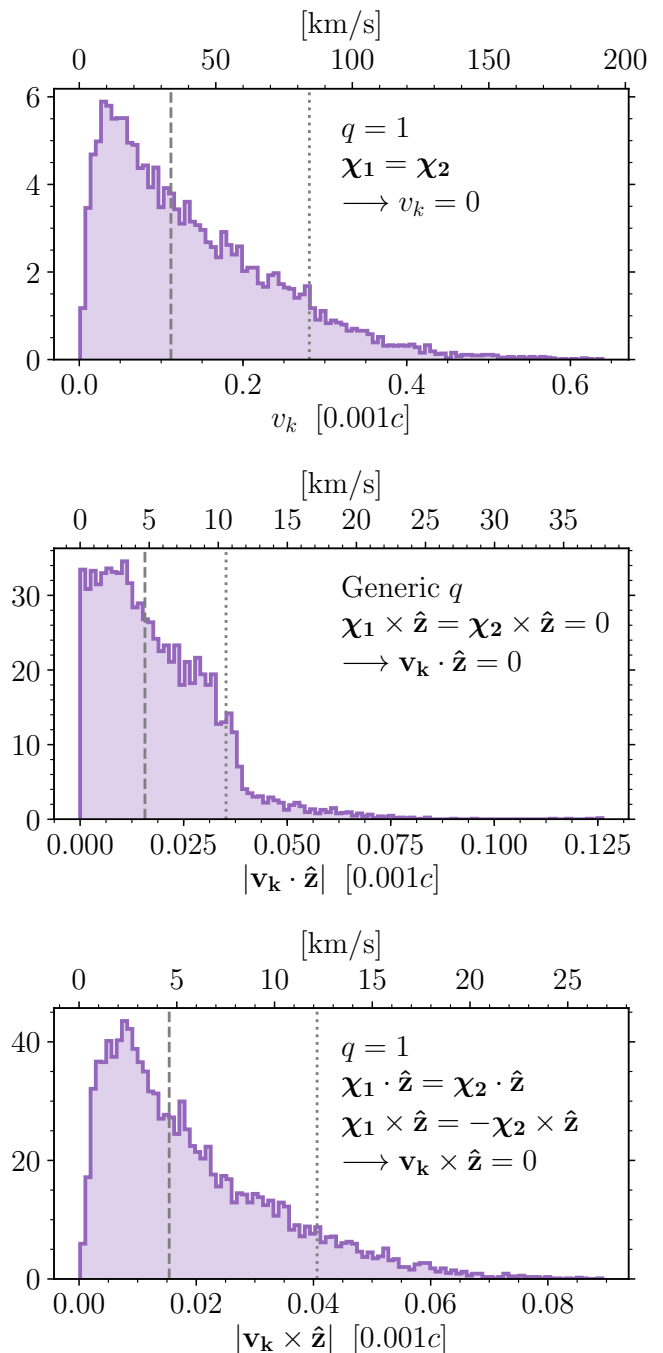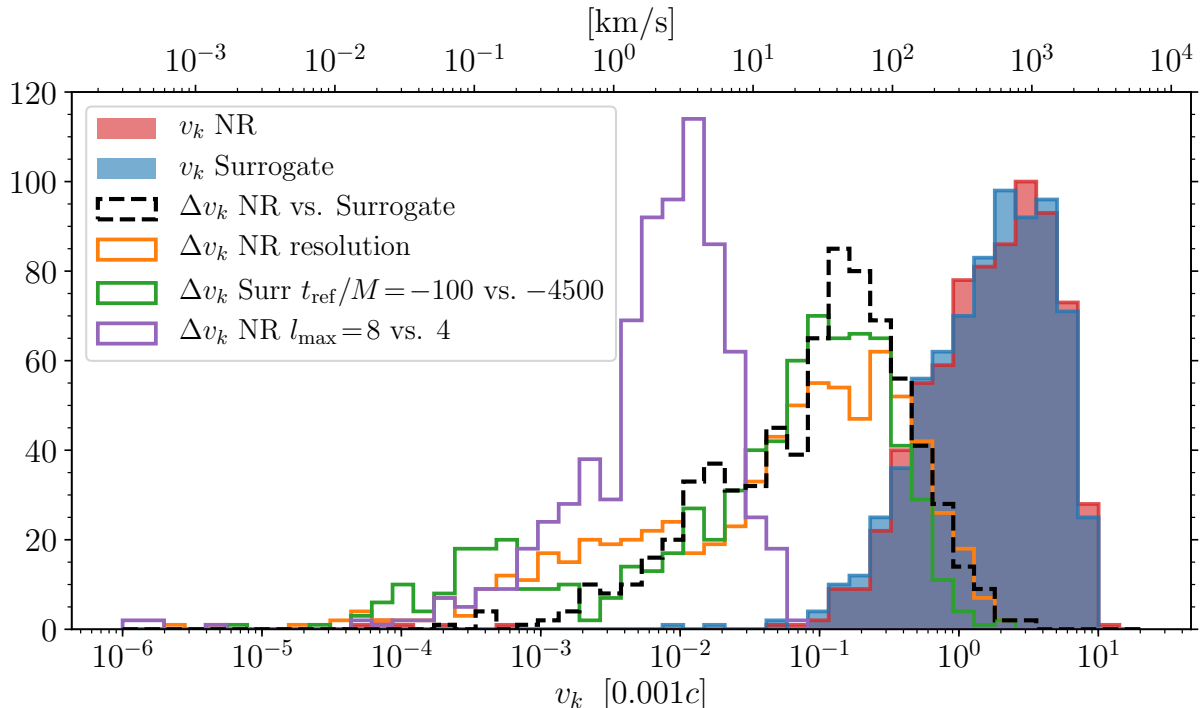

FIG. 11. Test of the kick numerical extraction by exploiting some of the symmetries of the system. All quantities shown in these plots are expected to be zero; deviations are interpreted as numerical inaccuracies of our extraction procedure. Top panel, symmetry (i): equal mass binaries with the same spin vectors are expected to have zero kicks. Middle panel, symmetry (ii): binaries with generic mass ratio and aligned spins are expected to have kicks in the orbital plane. Bottom panel, symmetry (iii): equal-mass binaries with opposite orbital-plane spin components and same aligned components are expected to have kicks directed along the binary's orbital angular momentum. Each panel contains a sample of 10^4 binaries generated as described in the text. Dashed (dotted) lines show medians (90th percentiles) of the distributions.

FIG. 12. Accuracy of the surrogate extraction of the kick velocity v_k compared to NR simulations from SpEC. Filled histograms show distributions of v_k extracted by both approaches, while the black dashed line shows residuals between the two methods. Solid thin lines explore some of the possible causes of the observed differences: the orange line shows a lower limit on the NR extraction accuracy, computed using the two highest resolutions available; the purple line shows residuals between NR kicks extracted with $l_{\max} = 8$ (default) and $l_{\max} = 4$ (corresponding to highest modes available in NRSur7dq2); the green line shows residuals in the surrogate extraction when the same NR runs are reproduced setting either $t_{\mathrm{ref}} = -100M$ or $t_{\mathrm{ref}} = -4500M$.

overlap between the interpolated and the NR strain h, not to accurately model BH kicks. The comparison to NR simulations will therefore be sensitive to errors from the surrogate's reproduction of the training set of gravitational waveforms, but insensitive to errors from the surrogate's interpolation between these waveforms.

Recoils are extracted from SpEC waveforms using the expressions reported in Sec. II B, and normalizing by the remnant mass computed from the BH horizon at the end of the SpEC simulation. We include modes up to $l_{\max} = 8$ from the highest resolution data. To compare with the surrogate kick, we must determine the correct binary parameters by first time-shifting and rotating the NR waveforms consistently with NRSur7dq2 (per criteria given in Sec. II A) and then measuring the BH spins at $t_{\mathrm{ref}} = -4500M$ as in [42]. Consequently the surrogate is evaluated with $t_{\mathrm{ref}} = -4500M$. Filled histograms in Fig. 12 show the distributions of v_k obtained for both the NR and surrogate extractions. Differences Δv_k between the two (thick dashed line) are typically $\sim 10^{-4}c$; 90% of the simulations are reproduced within $\Delta v_k = 5.5 \cdot 10^{-4}c$. On this histogram we also plot several sources of error to evaluate their importance. One of these is the difference between NR kicks extracted from different resolutions of each SpEC simulation — a solid upper limit on the accuracy of the NR kick extraction. This also presents a

tail up to $\sim 2 \cdot 10^{-3}c$, similar to that of Δv_k. The selection of the reference time t_{ref} in the surrogate extraction is a marginally smaller effect, with tail up to $\sim 10^{-3}c$. The contribution of higher-order modes $l > 4$ to the NR kick is a subdominant effect and contributes only on the scale of $\sim 10^{-5}c$. Finally, the error from evaluating the kick at a finite time $t = 100M$, instead of taking the kick's $t \to \infty$ limit, is negligible — the NR kicks extracted at $t = 100M$ and $135M$ (each simulation has a different final time in $[139M, 165M]$) differ by $\sim 10^{-8}c$ only.

The surrogate to NR comparison is also presented as a scatter plot in Fig. 13, which shows how the surrogate kick extraction faithfully reproduces the vast majority of the simulations. A few outliers with $\Delta v_k \sim 2 \cdot 10^{-3}c$ are present in the bottom-center of the figure (also in Fig. 12 as the tail of the Δv_k distribution), for which our surrogate extraction underestimates the value of v_k. These are cases where the surrogate model fails to correctly reproduce some cycles in the waveform's higher harmonics around the time of merger, when the majority of the kick is being accumulated. We note that cases with large Δv_k are preferentially located at the high-spin edge of the NRSur7dq2 parameter space: the three outliers mentioned above, and $\sim 2/3$ amongst the 5% of cases with largest Δv_k, have $\chi_1 = \chi_2 = 0.8$. This occurs because the error of the SpEC simulations, and consequently the surrogate
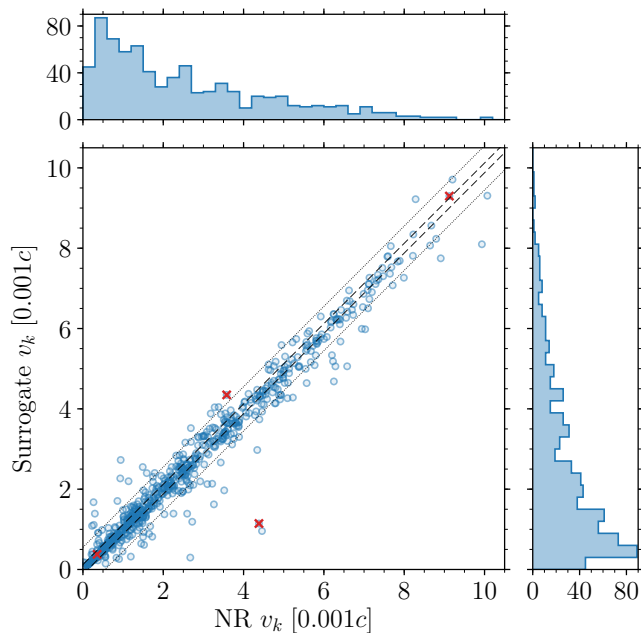
FIG. 13. Comparison between BH kicks extracted from NR SpEC simulations (horizontal) and surrogate model NRSur7dq2 (vertical). The NR runs used here are the same that entered the surrogate model calibration, which was not designed to model large kicks specifically. 50th and 90th percentiles are shown with dashed and dotted lines, respectively. Red crosses mark the four cases explored in Fig. 14.

model waveforms, increases towards this maximum-spin boundary. Restricting to the 464 NR simulations (or $\sim 2/3$ of the sample) with zero or one spin of magnitude $\chi = 0.8$, we find the surrogate reproduces 90% of the kicks within Δv_k of $3.8 \cdot 10^{-4}c \sim 113$ km/s. The error is about twice as large for the 280 simulations (or $\sim 1/3$ of the sample) with $\chi_1 = \chi_2 = 0.8$, with 90% of the kicks being within $7.7 \cdot 10^{-4}c \sim 232$ km/s.

Finally, Fig. 14 show comparisons for the kick accumulation profiles $\mathbf{P}(t) \cdot \hat{\mathbf{v}}_\mathbf{k}$ in four selected cases. We find the the surrogate model reproduces not only the kick magnitude v_k, but also the morphology of the time accumulation profile for the vast majority of the NR simulations. The lower left panel of Fig. 14 shows one of the few outliers, which presents $\Delta v_k \sim 3 \cdot 10^{-3}c$. The NR and surrogate profiles diverge around $t \sim 10M$, when the surrogate fails to capture the merger waveform. These two curves appear similar to the kick profiles of Fig. 7, suggesting the surrogate model fails to reconstruct the orbital phase at merger. Even if NRSur7dq2 well reproduces the strain h, its small errors might propagate to the phase of center of mass oscillation causing a relatively large error on the final kick velocity.

C. Comparison with numerical relativity simulations: LazEv.

Finally, we compare our results against NR simulations performed by the RIT group with the LazEv code [78]. This additional comparison is noteworthy because not only were these simulations not used in the surrogate calibration, but they were performed with a completely different numerical scheme (for a detailed comparison between SpEC and LazEv see [79]).

We compare against several series of simulations performed by Lousto and Zlochower that vary over the relative azimuthal projection of the spin (i.e. the angle α defined in Sec. III A) [40, 62]. Of the 223 NR simulations described in these references, 132 of them lie within the parameter range covered by NRSur7dq2.[4] We extract horizon masses, spins, and final kicks from the relevant tables in [40, 62], then we use the mass ratios and spins as inputs to NRSur7dq2. Case-by-case comparisons between the RIT simulations and the surrogate model are not possible because differences in gauges preclude us from converting their initial separations to our t_{ref}'s. We can, however, check for each case whether there exists a choice of t_{ref} for which the surrogate reproduces the reported value of the kick.

To this end, we rescale each of the RIT kick values $v_k^{(\text{NR})}$ with an affine transformation determined by the minimum and maximum surrogate kicks $v_k^{(\text{surr})}$ as t_{ref} is varied over the range $t_{\text{ref}}/M \in [-4500, -100]$, while holding all other parameters fixed:

$$\nu_k = \frac{v_k^{(\text{NR})} - \min_{t_{\text{ref}}} v_k^{(\text{surr})}}{\max_{t_{\text{ref}}} v_k^{(\text{surr})} - \min_{t_{\text{ref}}} v_k^{(\text{surr})}} . \quad (19)$$

Therefore the kicks from [40, 62] that can be reproduced lie in the range $0 \leq \nu_k \leq 1$. The resulting distribution of ν_k is shown in Fig. 15. We find that $0 \leq \nu_k \leq 1$ for $117/132 \simeq 89\%$ of the simulations. The remaining simulations cannot be matched by our procedure: in particular, the surrogate underestimates the NR result in $15/132 \simeq 11\%$ of the cases for which $\nu_k > 1$ (no simulations are found with $\nu_k < 0$). We stress, however, that these disagreements are very moderate, with $\nu_k < 1.12$ over all the simulations we analyzed.

The different comparisons presented in this section show that the surrogate kick extraction reaches precisions similar to those of the NR simulations that entered its calibration, well respects the symmetries of the problem, and matches kick results obtained with an independent NR code. We quote an overall average precision of 40 km/s on the surrogate extraction of v_k.

――――――

[4] Some of the simulations have parameters which exceed the range of validity of the surrogate model only very marginally ($q \simeq 0.498$ and/or $\chi_i \simeq 0.802$). We do not filter those runs out, but rather use NRSur7dq2 in extrapolation mode.
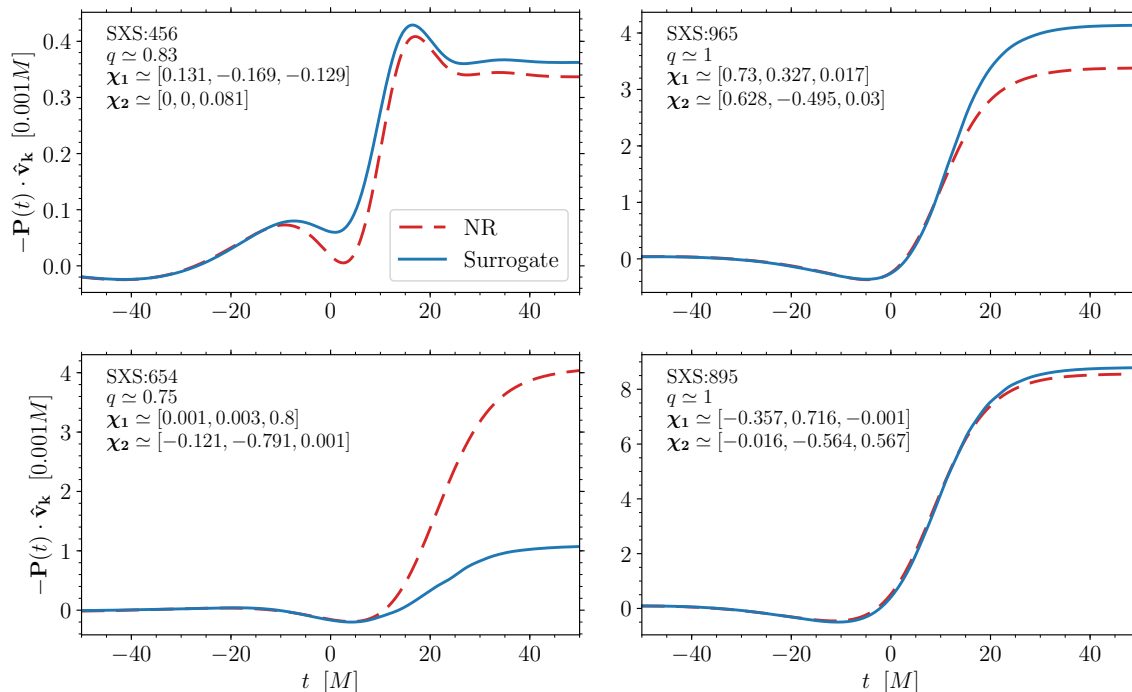
FIG. 14. Linear momentum profiles $\mathbf{P}(t)$ projected along the direction of the final kick $\hat{\mathbf{v}}_{\mathbf{k}}$ for four selected NR simulations from SpEC compared to predictions obtained with the surrogate model. These same four cases are marked with crosses in Fig. 13. While the vast majority of the kick morphologies are faithfully represented, some outliers are present. An example is provided in the bottom right panel, where profiles are in good agreement before merger but then diverge at $t \sim 10M$.
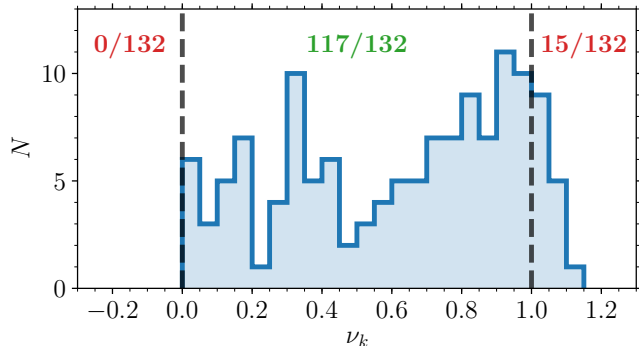
FIG. 15. Distribution of BH kicks extracted from 132 NR LazEV simulations [40, 62], rescaled between the minimum and maximum kick obtained from NRSur7dq2 [c.f. Eq. (19)]. If $0 \leq \nu_k \leq 1$, there exists a suitable choice of $t_{\rm ref}$ for which the surrogate model reproduces the NR value of the kick. On the other hand, the NR data cannot be reproduced if $\nu_k < 0$ or $\nu_k > 1$.

V. CODE DISTRIBUTION AND USAGE

Our numerical code, SURRKICK, is publicly available as a module for the Python programming language. The latest stable release is kept updated on the Python Package Index (PyPI) and can be installed via

```
pip install surrkick
```

Python packages numpy [80], scipy [81], matplotlib [82], h5py [83], pathos [84], tdqm [85], NRSur7dq2 [42] and precession [65] are specified as dependencies and will automatically be installed if missing. The SURRKICK module has to be imported with

```
import surrkick
```

from within a Python environment. Information on all classes, methods, and functions of the code can be obtained from the code docstrings using Python's `help` function. SURRKICK is hosted under version control on GitHub at github.com/dgerosa/surrkick, where development versions are available. Further information and code outputs can be found at davidegerosa.com/surrkick. SURRKICK is structured as an add-on to any waveform approximant. In particular, it will be straightforward to update it as new surrogate models become available. The code is currently compatible with Python 2; porting to Python 3 is foreseen. Results in this paper were obtained with version 1.1 of SURRKICK.

All the main functionalities of the code are provided as methods of a single class `surrkick.surrkick`. An instance of the class is created providing mass ratio q, spin vectors $\boldsymbol{\chi}_i$ and reference time $t_{\rm ref}/M$:

```
sk=surrkick.surrkick(q=1,chi1=[0,0,0],
            chi2=[0,0,0],t_ref=-100)
```

Method	Description	Equation	Default inputs
sur()	Instance of the surrogate class from NRSur7dq2.		
q	Binary mass ratio $q \in [0.5, 1]$.		$q = 1$.
chi1	Spin vector $\boldsymbol{\chi_1}$ of the heavier BH at t_{ref}.		$\boldsymbol{\chi_1} = [0,0,0]$.
chi2	Spin vector $\boldsymbol{\chi_2}$ of the lighter BH at t_{ref}.		$\boldsymbol{\chi_2} = [0,0,0]$.
t_ref	Reference time $t_{\mathrm{ref}}/M \in [-4500, -100]$.		$t_{\mathrm{ref}}/M = -100$.
times	Time nodes $t_i/M \in [-4500, 100]$.		
lmax	Largest available l-mode ($l_{\max} = 4$ in NRSur7dq2).		
h(l,m)	Modes of the complex GW strain h^{lm}.	Eq. (1)	
hdot(l,m)	Modes of the time derivative $\dot{h}^{lm}$		
dEdt	Energy flux dE/dt.	Eq. (2)	
Eoft	Radiated energy profile $E(t)$.		
Erad	Total radiated energy $\lim_{t\to\infty} E(t)$.		
Moft	Mass profile $M(t)$.	Eq. (4)	
Mrad	Mass of the remnant BH $\lim_{t\to\infty} M(t)$.		
Mfin	Mass of the remnant BH in units of the mass at $t = -\infty$.	Eq. (5)	
dPdt	Linear momentum flux $d\mathbf{P}/dt$	Eqs. (6-8)	
Poft	Radiated linear momentum profile $\mathbf{P}(t)$.		
Prad	Total radiated linear momentum $\lim_{t\to\infty} |\mathbf{P}(t)|$.		
voft	Recoil velocity profile $\mathbf{v}(t)$.	Eq. (13)	
kickcomp	Kick velocity, vector $\mathbf{v_k} = \lim_{t\to\infty} \mathbf{v}(t)$.	Eq. (14)	
kick	Kick velocity, magnitude v_k.		
kickdir	Kick velocity, unit vector $\hat{\mathbf{v}}_\mathbf{k} = \mathbf{v_k}/v_k$.		
dJdt	Angular momentum flux $d\mathbf{J}/dt$.	Eqs. (15-17)	
Joft	Radiated angular momentum profile $\mathbf{J}(t)$.		
Jrad	Total radiated angular momentum $\lim_{t\to\infty} |\mathbf{J}(t)|$.		
xoft	Center-of-mass trajectory $\mathbf{x}(t) = \int \mathbf{v}(t)dt$.		

TABLE I. Main methods of the surrkick class. A class instance has to be initialized with e.g. sk=surrkick.surrkick(q=1,chi1=[0,0,0],chi2=[0,0,0],t_ref=-100). Methods can then be accessed with e.g. sk.voft.

A list of the relevant methods is provided in Table I. All quantities are returned in units of the binary's total mass (i.e. $c = G = M = 1$). Time profiles are evaluated at the time nodes sk.times. For instance, the following code snippet computes the final kick imparted to a right-left binary with $q = 0.5$ and $\chi_1 = \chi_2 = 0.8$, and plots the velocity profile $\mathbf{v}(t)$ projected along $\hat{\mathbf{x}}, \hat{\mathbf{y}}, \hat{\mathbf{z}}$ and $\hat{\mathbf{v}}_\mathbf{k}$.

```
import surrkick
import matplotlib.pyplot as plt
sk=surrkick.surrkick(q=0.5,chi1=[0.8,0,0],
    chi2=[-0.8,0,0])
print "vk/c=", sk.kick
plt.plot(sk.times,sk.voft[:,0],label="x")
plt.plot(sk.times,sk.voft[:,1],label="y")
plt.plot(sk.times,sk.voft[:,2],label="z")
plt.plot(sk.times,surrkick.project(sk.voft,
    sk.kickdir),label="vk")
plt.xlim(-100,100)
plt.legend()
plt.show()
```

The class surrkick.plots provides tools to reproduce all figures and results presented in this paper. The snippet above is implemented as surrkick.plots.minimal().

Performance of the code was evaluated on a single processor of an Intel Xeon CPU E5-2660 v3 @2.60GHz averaging over 10^3 binaries with generic parameters. Computation of v_k takes ~ 0.1 s, where ~ 50 ms are spent evaluating h from NRSur7dq2 [42] and ~ 50 ms are spent integrating the energy and linear momentum fluxes. These low executions times make our code ideal to be ported into large-scale computational studies.

VI. CONCLUSIONS

New waveform approximants able to model precessing BH binaries with higher harmonics have been recently developed for GW detection and parameter estimation. Here we show, for the first time, how these tools present an interesting by-product, namely the quick and reliable estimation of energy and momenta radiated in GWs during BH inspirals and mergers. In particular, dissipation of linear momentum is responsible for powerful BH recoils,

which might even eject BHs from their host galaxies. We exploited the recent NR surrogate model NRSur7dq2 [42] to explore the phenomenology of the recoil velocity profile $\mathbf{v}(t)$ that generic binaries are imparted as they merge. Our findings are implemented in the numerical code SURRKICK, which is made available to the community as a module for the Python programming language.

Our extraction procedure inherits both strengths and weaknesses of NRSur7dq2. The model can reproduce the GW strain with mismatches $\sim 10^{-3}$, orders of magnitude better than any other model currently available. This translates into an average accuracy $\Delta v_k/c \lesssim 10^{-4}$ on the recoil estimates. The model has only been calibrated on BH binaries with mass ratios $q \geq 0.5$ and spin magnitudes $\chi_i \leq 0.8$. Both NRSur7dq2 and SURRKICK can in principle be used outside this range, but those extrapolations have not been tested accurately. NRSur7dq2 provides evolutions over a time $\Delta t \sim 5000M$, corresponding to ~ 20 orbits before merger. While this is a severe limitation for waveform modeling (because low-mass systems spend many more cycles in the sensitivity windows of the detectors), it is irrelevant for kick estimation. Linear momentum emission is concentrated on a small time window ($2\sigma \sim 20M$) around merger which is well covered by NRSur7dq2.

The tools presented here provide an alternative way to estimate BH kicks which, contrary to fitting formulae, does not require specific ansätze. Moreover, they provide information on the full $\mathbf{v}(t)$ profile, not just the final recoil velocity v_k. With executions times of ~ 0.1 s, our approach allows for quick and reliable implementations of BH kicks in a variety of astrophysical studies, from galaxy evolution codes to population synthesis studies of compact binaries. Future developments include building new NR surrogate models specifically designed to accurately reproduce mass, spin, and recoil of the post-merger BH.

[1] J. H. Taylor and J. M. Weisberg, ApJ **253**, 908 (1982).

[2] Abbott, B. P. *et al.* (LIGO and Virgo Scientific Collaboration), PRL **116**, 061102 (2016), arXiv:1602.03837 [gr-qc].

[3] W. B. Bonnor and M. A. Rotenberg, Proceedings of the Royal Society of London Series A **265**, 109 (1961).

[4] A. Peres, Physical Review **128**, 2471 (1962).

[5] M. J. Fitchett, MNRAS **203**, 1049 (1983).

[6] L. E. Kidder, PRD **52**, 821 (1995), gr-qc/9506022.

[7] L. Blanchet, M. S. S. Qusailah, and C. M. Will, ApJ **635**, 508 (2005), astro-ph/0507692.

[8] F. Pretorius, Physical Review Letters **95**, 121101 (2005), gr-qc/0507014.

[9] M. Campanelli, C. O. Lousto, P. Marronetti, and Y. Zlochower, Physical Review Letters **96**, 111101 (2006), gr-qc/0511048.

[10] J. G. Baker, J. Centrella, D.-I. Choi, M. Koppitz, and J. van Meter, Physical Review Letters **96**, 111102 (2006), gr-qc/0511103.

[11] M. Campanelli, C. O. Lousto, Y. Zlochower, and D. Merritt, PRL **98**, 231102 (2007), gr-qc/0702133.

[12] J. A. González, M. Hannam, U. Sperhake, B. Brügmann, and S. Husa, PRL **98**, 231101 (2007), gr-qc/0702052.

[13] W. Tichy and P. Marronetti, PRD **76**, 061502 (2007), gr-qc/0703075.

[14] C. O. Lousto and Y. Zlochower, PRL **107**, 231102 (2011), arXiv:1108.2009 [gr-qc].

[15] A. Sesana, MNRAS **382**, L6 (2007), arXiv:0707.4677.

[16] J. D. Schnittman and A. Buonanno, ApJ **662**, L63 (2007), astro-ph/0702641.

[17] A. Gualandris and D. Merritt, ApJ **678**, 780-797 (2008), arXiv:0708.0771.

[18] G. A. Shields and E. W. Bonning, ApJ **682**, 758-766 (2008), arXiv:0802.3873.

[19] K. Holley-Bockelmann, K. Gültekin, D. Shoemaker, and N. Yunes, ApJ **686**, 829-837 (2008), arXiv:0707.1334.

[20] L. Blecha and A. Loeb, MNRAS **390**, 1311 (2008), arXiv:0805.1420.

[21] D. Merritt, M. Milosavljević, M. Favata, S. A. Hughes, and D. E. Holz, ApJ **607**, L9 (2004), astro-ph/0402057.

[22] D. Gerosa and A. Sesana, MNRAS **446**, 38 (2015), arXiv:1405.2072.

[23] I. H. Redmount and M. J. Rees, Comments on Astrophysics **14**, 165 (1989).

[24] S. Komossa, Advances in Astronomy **2012**, 364973 (2012), arXiv:1202.1977 [astro-ph.CO].

[25] S. Komossa, H. Zhou, and H. Lu, ApJ **678**, L81 (2008), arXiv:0804.4585.

[26] F. Civano, M. Elvis, G. Lanzuisi, T. Aldcroft, M. Trichas, A. Bongiorno, M. Brusa, L. Blecha, A. Comastri, A. Loeb, *et al.*, ApJ **752**, 49 (2012), arXiv:1205.0815.

[27] R. Decarli, M. Dotti, C. Mazzucchelli, C. Montuori, and M. Volonteri, MNRAS **445**, 1558 (2014), arXiv:1409.1585.

[28] M. Koss, L. Blecha, R. Mushotzky, C. L. Hung, S. Veilleux, B. Trakhtenbrot, K. Schawinski, D. Stern, N. Smith, Y. Li, *et al.*, MNRAS **445**, 515 (2014), arXiv:1401.6798.

[29] M. Chiaberge, J. C. Ely, E. T. Meyer, M. Georganopoulos, A. Marinucci, S. Bianchi, G. R. Tremblay, B. Hilbert, J. P. Kotyla, A. Capetti, *et al.*, A&A **600**, A57 (2017), arXiv:1611.05501.

[30] D.-C. Kim, I. Yoon, G. C. Privon, A. S. Evans, D. Harvey, S. Stierwalt, and J. H. Kim, ApJ **840**, 71 (2017), arXiv:1704.05549.

[31] E. Kalfountzou, M. Santos Lleo, and M. Trichas, ApJ **851**, L15 (2017), arXiv:1712.03909.

[32] D. Lena, A. Robinson, A. Marconi, D. J. Axon, A. Capetti, D. Merritt, and D. Batcheldor, ApJ **795**, 146 (2014), arXiv:1409.3976.

[33] P. Raffai, Z. Haiman, and Z. Frei, MNRAS **455**, 484 (2016), arXiv:1509.02075.

[34] L. Blecha, D. Sijacki, L. Z. Kelley, P. Torrey, M. Vogelsberger, D. Nelson, V. Springel, G. Snyder, and L. Hernquist, MNRAS **456**, 961 (2016), arXiv:1508.01524.

[35] D. Gerosa and C. J. Moore, PRL **117**, 011101 (2016), arXiv:1606.04226 [gr-qc].

[36] M. Campanelli, C. Lousto, Y. Zlochower, and D. Merritt, ApJ **659**, L5 (2007), gr-qc/0701164.

[37] J. A. González, U. Sperhake, B. Brügmann, M. Hannam, and S. Husa, PRL **98**, 091101 (2007), gr-qc/0610154.

[38] C. O. Lousto and Y. Zlochower, PRD **77**, 044028 (2008), arXiv:0708.4048 [gr-qc].

[39] C. O. Lousto, Y. Zlochower, M. Dotti, and M. Volonteri, PRD **85**, 084015 (2012), arXiv:1201.1923 [gr-qc].

[40] C. O. Lousto and Y. Zlochower, PRD **87**, 084027 (2013), arXiv:1211.7099 [gr-qc].

[41] B. Brügmann, J. A. González, M. Hannam, S. Husa, and U. Sperhake, PRD **77**, 124047 (2008), arXiv:0707.0135 [gr-qc].

[42] J. Blackman, S. E. Field, M. A. Scheel, C. R. Galley, C. D. Ott, M. Boyle, L. E. Kidder, H. P. Pfeiffer, and B. Szilágyi, PRD **96**, 024058 (2017), arXiv:1705.07089 [gr-qc].

[43] K. S. Thorne, Reviews of Modern Physics **52**, 299 (1980).

[44] S. E. Field, C. R. Galley, J. S. Hesthaven, J. Kaye, and M. Tiglio, PRX **4**, 031006 (2014), arXiv:1308.3565 [gr-qc].

[45] M. Pürrer, CQG **31**, 195010 (2014), arXiv:1402.4146 [gr-qc].

[46] M. Pürrer, PRD **93**, 064041 (2016), arXiv:1512.02248 [gr-qc].

[47] J. Blackman, S. E. Field, M. A. Scheel, C. R. Galley, D. A. Hemberger, P. Schmidt, and R. Smith, PRD **95**, 104023 (2017), arXiv:1701.00550 [gr-qc].

[48] L. E. Kidder, M. A. Scheel, S. A. Teukolsky, E. D. Carlson, and G. B. Cook, PRD **62**, 084032 (2000), gr-qc/0005056.

[49] M. Ruiz, M. Alcubierre, D. Núñez, and R. Takahashi, GRG **40**, 1705 (2008), arXiv:0707.4654 [gr-qc].

[50] C. O. Lousto and Y. Zlochower, PRD **76**, 041502 (2007), gr-qc/0703061.

[51] É. É. Flanagan and D. A. Nichols, PRD **95**, 044002 (2017), arXiv:1510.03386 [hep-th].

[52] P. C. Peters, Physical Review **136**, 1224 (1964).

[53] K. G. Arun, A. Buonanno, G. Faye, and E. Ochsner, PRD **79**, 104023 (2009), [Erratum: PRD 84, 049901 (2011)], arXiv:0810.5336 [gr-qc].

[54] L. Rezzolla, R. P. Macedo, and J. L. Jaramillo, PRL **104**, 221101 (2010), arXiv:1003.0873 [gr-qc].

[55] D. Gerosa, M. Kesden, R. O'Shaughnessy, A. Klein, E. Berti, U. Sperhake, and D. Trifirò, PRL **115**, 141102 (2015), arXiv:1506.09116 [gr-qc].

[56] T. Damour, PRD **64**, 124013 (2001), gr-qc/0103018.

[57] M. Campanelli, C. O. Lousto, and Y. Zlochower, PRD **74**, 041501 (2006), gr-qc/0604012.

[58] M. A. Scheel, M. Giesler, D. A. Hemberger, G. Lovelace, K. Kuper, M. Boyle, B. Szilágyi, and L. E. Kidder, CQG **32**, 105009 (2015), arXiv:1412.1803 [gr-qc].

[59] J. G. Baker, W. D. Boggs, J. Centrella, B. J. Kelly, S. T. McWilliams, M. C. Miller, and J. R. van Meter, ApJ **668**, 1140 (2007), astro-ph/0702390.

[60] L. Boyle, M. Kesden, and S. Nissanke, PRL **100**, 151101 (2008), arXiv:0709.0299 [gr-qc].

[61] L. Boyle and M. Kesden, PRD **78**, 024017 (2008), arXiv:0712.2819.

[62] Y. Zlochower and C. O. Lousto, PRD **92**, 024022 (2015), [Erratum: PRD 94, 029901 (2016)], arXiv:1503.07536 [gr-qc].

[63] E. M. Rossi, G. Lodato, P. J. Armitage, J. E. Pringle, and A. R. King, MNRAS **401**, 2021 (2010), arXiv:0910.0002 [astro-ph.HE].

[64] L. R. Corrales, Z. Haiman, and A. MacFadyen, MNRAS **404**, 947 (2010), arXiv:0910.0014 [astro-ph.HE].

[65] D. Gerosa and M. Kesden, PRD **93**, 124066 (2016), arXiv:1605.01067 [astro-ph.HE].

[66] U. Sperhake, in *Gravitational Wave Astrophysics*, Astrophysics and Space Science Proceedings, Vol. 40 (2015) p. 185.

[67] J. G. Baker, W. D. Boggs, J. Centrella, B. J. Kelly, S. T. McWilliams, M. C. Miller, and J. R. van Meter, ApJ **682**, L29 (2008), arXiv:0802.0416.

[68] C. O. Lousto and Y. Zlochower, PRD **79**, 064018 (2009), arXiv:0805.0159 [gr-qc].

[69] E. Barausse, V. Morozova, and L. Rezzolla, ApJ **758**, 63 (2012), arXiv:1206.3803 [gr-qc].

[70] X. Jiménez-Forteza, D. Keitel, S. Husa, M. Hannam, S. Khan, and M. Pürrer, PRD **95**, 064024 (2017), arXiv:1611.00332 [gr-qc].

[71] J. M. Bardeen and J. A. Petterson, ApJ **195**, L65 (1975).

[72] P. Hut, A&A **99**, 126 (1981).

[73] G. Lodato and D. Gerosa, MNRAS **429**, L30 (2013), arXiv:1211.0284.

[74] M. C. Miller and J. H. Krolik, ApJ **774**, 43 (2013), arXiv:1307.6569 [astro-ph.HE].

[75] D. Gerosa, B. Veronesi, G. Lodato, and G. Rosotti, MNRAS **451**, 3941 (2015), arXiv:1503.06807.

[76] M. Kesden, U. Sperhake, and E. Berti, ApJ **715**, 1006 (2010), arXiv:1003.4993 [astro-ph.CO].

[77] A. H. Mroué, M. A. Scheel, B. Szilágyi, H. P. Pfeiffer, M. Boyle, D. A. Hemberger, L. E. Kidder, G. Lovelace, S. Ossokine, N. W. Taylor, A. Zenginoğlu, L. T. Buchman, T. Chu, E. Foley, M. Giesler, R. Owen, and S. A. Teukolsky, PRL **111**, 241104 (2013), arXiv:1304.6077 [gr-qc].

[78] Y. Zlochower, J. G. Baker, M. Campanelli, and C. O. Lousto, PRD **72**, 024021 (2005), gr-qc/0505055.

[79] G. Lovelace, C. O. Lousto, J. Healy, M. A. Scheel, A. Garcia, R. O'Shaughnessy, M. Boyle, M. Campanelli, D. A. Hemberger, L. E. Kidder, H. P. Pfeiffer, B. Szilágyi, S. A. Teukolsky, and Y. Zlochower, Classical and Quantum Gravity **33**, 244002 (2016), arXiv:1607.05377 [gr-qc].

[80] S. van der Walt, S. Colbert, and G. Varoquaux, Computing in Science Engineering **13**, 22 (2011).

[81] E. Jones, T. Oliphant, P. Peterson, *et al.*, "SciPy: Open source scientific tools for Python," http://www.scipy.org/ (2001–).

[82] J. D. Hunter, Computing in Science and Engineering **9**, 90 (2007).

[83] A. Collette, *Python and HDF5* (O'Reilly, 2013).

[84] M. M. McKerns, L. Strand, T. Sullivan, A. Fang, and M. A. Aivazis, in *Proceedings of the 10th Python in Science Conference*, edited by S. van der Walt and J. Millman (2011) pp. 67 – 78, 1202.1056 [cs.MS].

[85] C. da Costa-Luis *et al.*, Zenodo (2017), 10.5281/zenodo.1012577.